Supplementary Material for "Geometry and Length Control of 3D Engineered Heart Tissues Using Direct Laser Writing"

M. Ç. Karakan,[1,2,3,4,*] J. K. Ewoldt,[3,4] A. Segarra,[2] S. Sundaram,[3,4] M. C. Wang,[3,4,5] C. S. Chen,[3,4] A. E. White,[1,2,3,6,7] and K. L. Ekinci[1,2,6]

[1]*Department of Mechanical Engineering, Boston University, Boston, Massachusetts 02215, USA*
[2]*Photonics Center, Boston University, Boston, MA 02215, USA.*
[3]*Department of Biomedical Engineering, Boston University, Boston, Massachusetts 02215, USA*
[4]*Wyss Institute for Biologically Inspired Engineering, Harvard University, Boston, MA 02115, USA.*
[5]*Harvard-MIT Program in Health Sciences and Technology, Institute for Medical Engineering and Science, Massachusetts Institute of Technology, Cambridge, MA 02139, USA*
[6]*Division of Materials Science and Engineering, Boston University, Boston, Massachusetts 02215, USA*
[7]*Department of Physics, Boston University, Boston, MA 02215, USA.*

(Dated: January 14, 2024)

Contents

I. Mold Design and Fabrication 2

II. Two-photon Direct Laser Writing of the Attachment Sites 3

III. Simulated Spring Constant of the Devices 4

IV. Remodeling of the Engineered Heart Tissues in Stadium-like Cavities 4

V. Fiber Alignment Inside the Stable Tissues 5

VI. Contractile Displacements in 2D 5

VII. Experiment with the GSB-L550 Cell Line 6

VIII. Effect of the Cage Length on Contractile Force 7

IX. Calcium Dynamics 9

X. Supplementary Movies 12
A. Movie S1 12
B. Movie S2 12
C. Movie S3 12
D. Movie S4 12
E. Movie S5 12

References 13

*Electronic mail:karakan@bu.edu

I. MOLD DESIGN AND FABRICATION

Figure S1 illustrates the design of the mold. Figure S1A displays the entire mold and Figure S1B represents a unit chip. Each mold is designed to have four chips, and each chip is designed to have 2 × 4 individual seeding wells with 0.8 mm, 1 mm, 1.2 mm, and 1.4 mm lengths. Figure S1C shows an isometric view, Fig. S1D shows the cross section of the mold to generate an individual 1.2 mm long elongated cylindrical cavity. The 25 μm-thick membranes of the seeding well are designed to be generated by the thin openings in the shell. The thicker openings and longer designs are for elongating and sealing the opening wells with the PDMS. In a similar fashion, Fig. S1E shows a rendering of another design with rectangular cavities, which is designed to fabricate 2 × 2 unit chips with 8 individual cavities to generate a pair of tissues with 0.5 mm, 1 mm, 1.5 mm, and 2 mm (see Fig. S1F). Fig. S1G shows a cross-sectional view of a mold design to generate a 1 mm long EHT. As one can observe by comparing Fig. S1D and Fig. S1G, the two designs have a very similar nature, but the rectangular design allows for the generation of tissues with higher aspect ratios. Another important parameter to note is the height of the membranes and the cavity itself. In this chapter, heights were tuned between 0.3 and 0.4 mm for the membranes, and between 0.5 and 0.6 mm for the seeding wells. Some expected properties and parameters of the designs are presented in Table 1 in the main text.

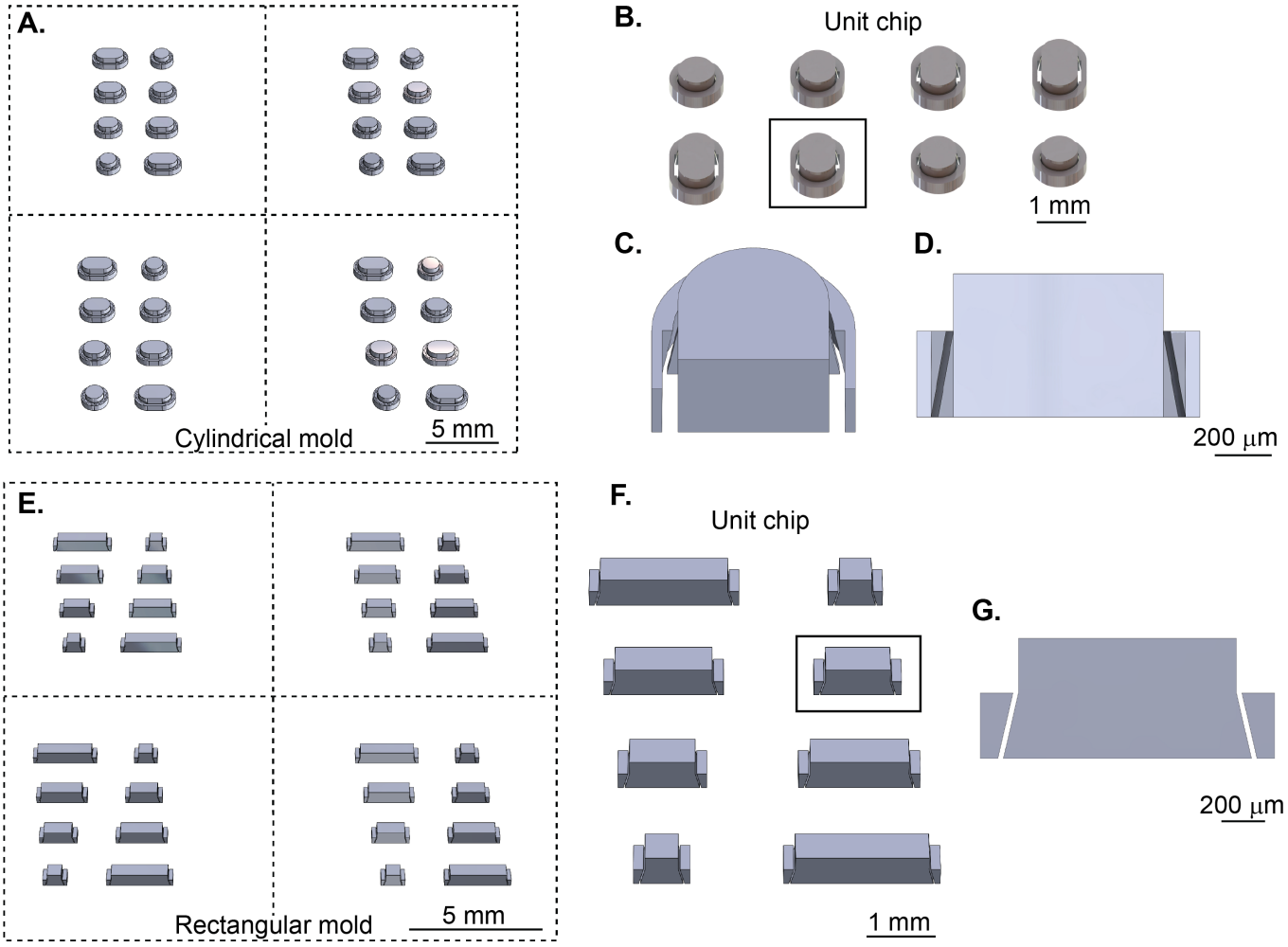

FIG. S1: Mold design. (A) Design of the cylindrical mold. (B) Design of a cylindrical mold for a unit chip. (C) Isometric view of a cross-sectional cut from a 400 μm elongated circular mold. (D) Front view of a cross-sectional cut from an elongated mold for generating an individual seeding well. (E) Design of a rectangular mold for a unit chip. (F) Design of a cylindrical mold for a unit chip. (G) Front view of a cross-sectional view from a rectangular mold to fabricate an individual seeding well for a 1 mm long EHT.

Before printing the mold, silicon substrates (University Wafer, Boston, MA) were cut to 25 mm × 25 mm for the rectangular and 30 mm × 30 mm for the stadium-like seeding wells. After cleaning, substrates were plasma-treated (Harrick Plasma Cleaner) in air with 10.5 W RF power for at least a minute, then placed in a vacuum desiccator

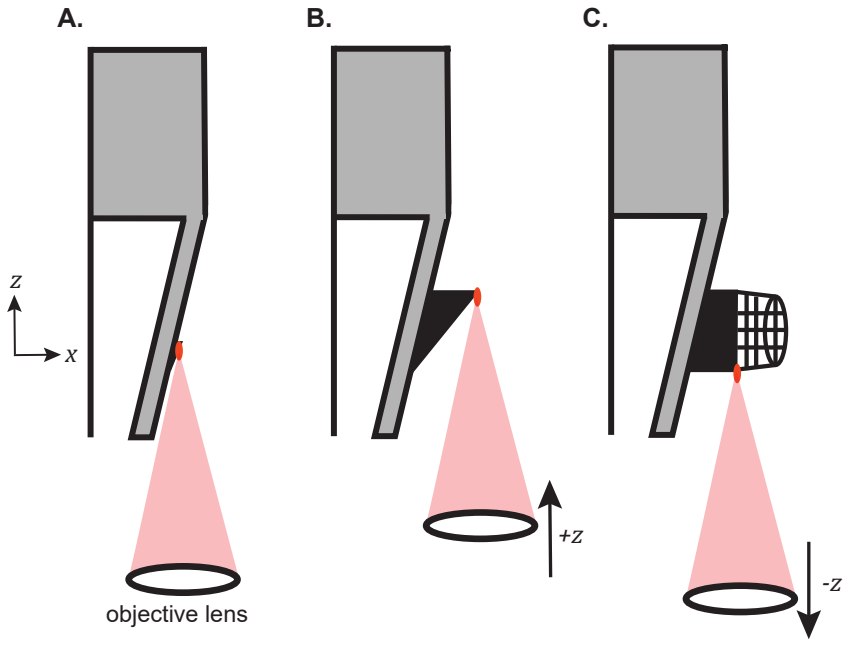

FIG. S2: DLW of an attachment site. After focusing on the bottom surface of the membrane, the objective was moved 100 or 150 μm along the z axis, and $100\tan(10°)$ or $150\tan(10°)$ μm in the x direction (A). Next, the diagonal half of the stub is printed by moving the objective in the z direction and scanning the laser in x and y directions (B). The DLW of attachment sites is completed by printing the overhanging part onto the anchors by moving the objective in the $-z$ direction (C).

chamber, along with a few droplets of 3(trimethoxysilyl)propyl acrylate (TMPA) on a glass slide. After waiting for at least 12 hours to ensure that the surface was functionalized, the chips were stored until printing. IP-S photoresist (Nanoscribe) was used as the mold material. The molds were printed using shell and scaffold mode with tetrahedral scaffolds to optimize the speed of printing. The slicing distance was 1.8 μm and the hatching distance was 0.8 μm. The structures were printed as $270 \times 270 \times 300$ μm^3 rectangular blocks to fit into the scan field of the 25 × objective, and these blocks were stitched together by defining 13° shear angle to the blocks and 2 μm overlap between the blocks. The entire structure was printed with a constant velocity of 130 mm/s and constant power of 88%. After the printing process (Fig. 1A-i), the residual resist was removed from the molds by placing the chips into a propylene glycol monomethyl ether acetate (PGMEA) bath for between 3-6 hours. After rinsing, the remaining PGMEA is cleaned from the mold by dipping the samples into a NOVEC 7100 (3M) bath and slowly removing the sample. To solidify the unpolymerized resist trapped in the body, the molds were exposed to a UV light source (5W, 389 nm, Prizmatix) for 20-50 seconds. Molds were plasma treated and subsequently fluorinated using trichloro-(1H,2H,2H-perfluorooctyl) silane (TPFOS, Sigma) to minimize the adhesion between PDMS and the mold (red color in Fig. 1A-ii).

II. TWO-PHOTON DIRECT LASER WRITING OF THE ATTACHMENT SITES

Cage printing is implemented as a two-step process. After finding the top surface and edges of the membranes, the objective was moved 100-150 μm into the resist to ensure the printing of attachment sites at the center of the membranes (Fig.S2A). First, we started with the DLW of the diagonal half of the stubs. We programmed the objective to move upward during this writing step. After the end of this step, the half-stubs with 45° angle provided an anchor to print the rest of the stub, and the overhang structures. In the second step, the objective was moved downward to print the rest of the construct, with some overlap to ensure robust attachment and provide an effectively monolithic structure for cells. After the printing process, PDMS samples were sequentially rinsed in Propylene glycol methyl ether acetate (PGMEA) (2 minutes), ethanol (2 minutes), isopropanol (4 minutes), and DI water.

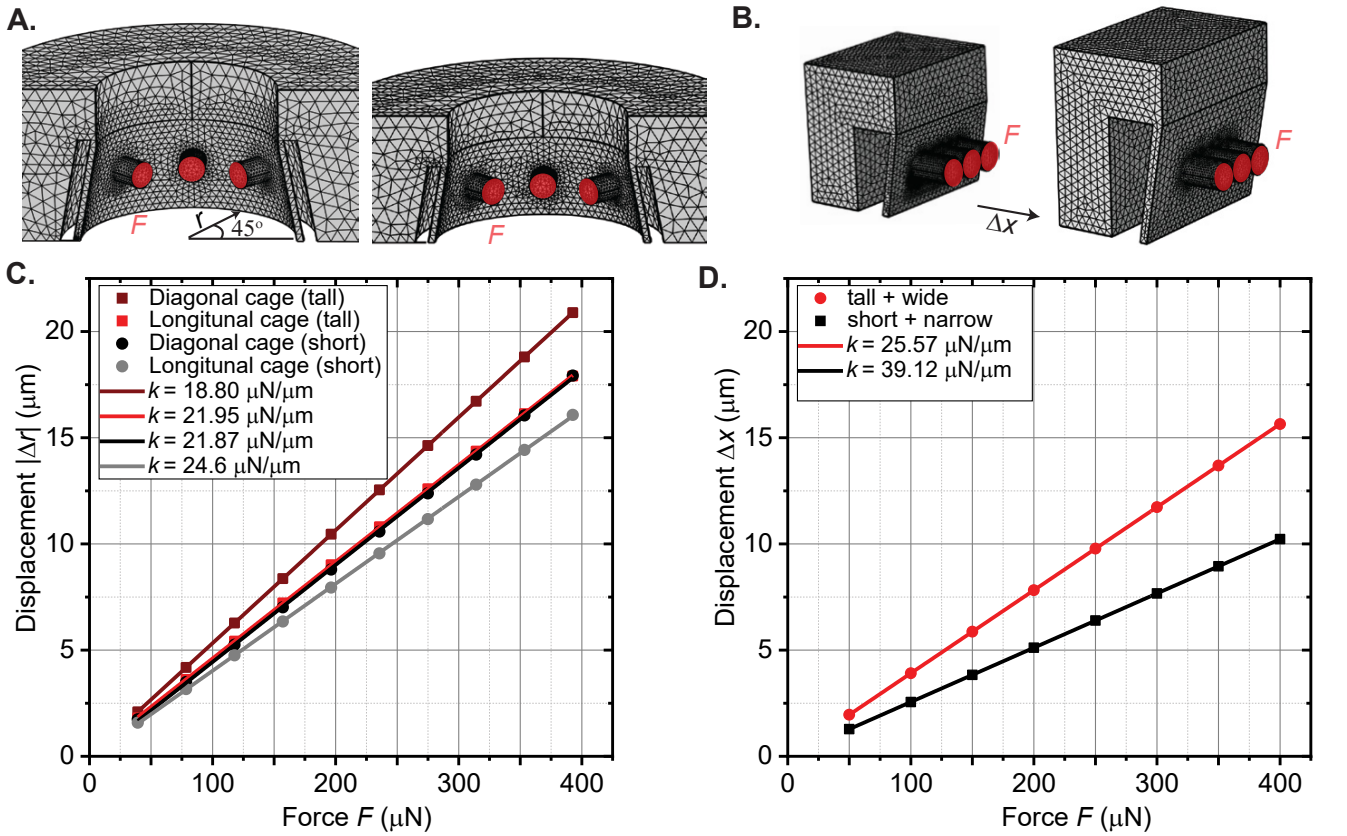

FIG. S3: Spring constant of the devices, estimated from finite element models. (A) and (B) shows the finite element models of the stadium-like and uniaxial devices respectively, where short and tall versions of the device are side by side. Meshes are generated with free tetrahedral elements, and forces are applied upon the red-shaded regions along the normally outward direction. (C) and (D) show the displacements $|\Delta r|$ and Δx observed in the simulations upon application of the forces F.

III. SIMULATED SPRING CONSTANT OF THE DEVICES

We developed finite element models to estimate the effective spring constant of the platform in different configurations. Material properties used in these simulations are based on experimentally verified prior work [1], geometry and dimensions are based on the dimensions of the molds and the placement of direct-laser-written attachment sites. Fig. S3 summarizes the result of simulations. For cylindrical and stadium-like configurations, we applied 5-50 kPa normal stress outward from the red-shared region in 5 kPa increments, equal to $\sim 40-400$ μN according to $F = \sigma A$. For uniaxial configuration, we applied a force between $40-400$ μN in 50 μN increments. Displacements we observed in $-r$ and x directions are plotted and spring constants k are estimated by applying a linear fit and equating the slope to k^{-1}.

IV. REMODELING OF THE ENGINEERED HEART TISSUES IN STADIUM-LIKE CAVITIES

To investigate the impact of the length and aspect ratio within another geometric context, we observed the remodeling of EHTs generated in the stadium-like cavities. Fig. S4A-D shows the remodeling of tissue morphology between Day 2 and Day 9 for tissues with lengths of 0.8 mm, 1 mm, 1.2 mm, and 1.4 mm and aspect ratios of 1.6, 2, 2.4, and 2.8 respectively. Here, we again observed the necking phenomenon, correlated with the increased length and aspect ratios. Fig. S4D displays a 1.4 mm long symmetric tissue, and Fig. S4E represents another 1.4 mm long EHT with a missing diagonal cage. We compared the tissue remodeling in these tissues to explore the effect of asymmetry and loss of a single attachment site on the remodeling of the EHTs. Surprisingly, the asymmetrically engineered heart tissue had a wider neck and appeared to be more stable than the symmetric EHT.

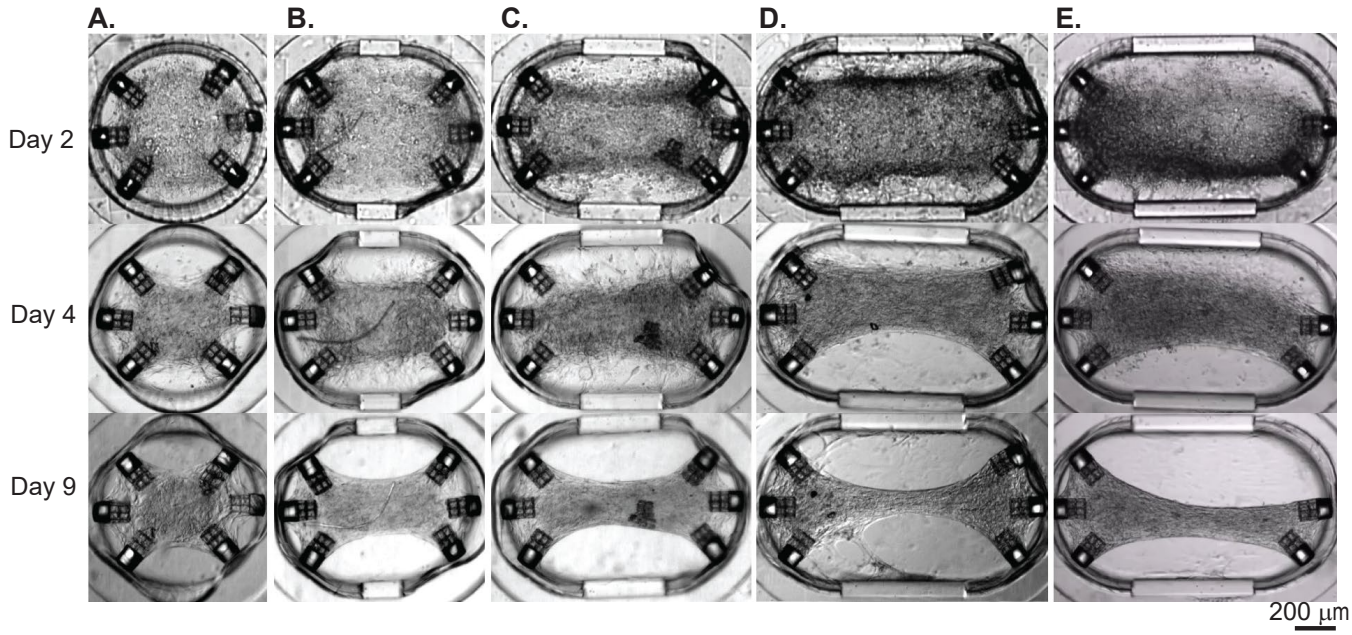

FIG. S4: Tissue remodeling and necking inside stadium-like cavities. Tissue remodeling for a (A) 0.8 mm, (B) 1 mm, (C) 1.2 mm, and (D) 1.4 mm long tissue generated in cylindrical cavities over the course of 8 days. (E) shows a 1.4 mm long asymmetric tissue to demonstrate how attachment sites affect tissue remodeling.

V. FIBER ALIGNMENT INSIDE THE STABLE TISSUES

After forming stable tissue constructs, we explored fiber structures inside these tissues. Fig. S5A-D shows multi-plane projected confocal micrographs of the wide EHTs suspended between 0° and diagonally-placed attachment sites. Unlike the previous iteration, we did not observe an increase in the degree of alignment as the tissues were scaled up in both aspect ratio and number of cells. The fibers in these EHTs look aligned at the corners and the edges, but the alignment at the center of these tissues remained random as the tissue length is increased by 0.2 mm increments. We also made some observations regarding the thickness of these EHTs. The orthogonal projection of the images, shown in Fig. S5E, suggests that the tissues had an ellipsoidal cross-section which was thicker at the center.

Fig. S6A-D shows representative confocal projections taken from centers of 0.5 mm, 1 mm, 1.5 mm, and 2 mm long EHTs. Visual inspection showed that the fibers at the edges appear to be more aligned than the fibers at the center, especially as the length of the tissue was increased. To assess and compare the fiber alignment at the cores of these tissues, higher magnification images are shown in Fig. S6E-H. Here, most fibers were distributed randomly at the center for all cases except in Fig. S6H, where there was a subtle alignment in the direction imposed by the tissue boundaries. Fig. S6I highlights a difference we observed in the alignment of the sarcomeres between the center and edge regions of a 2 mm long EHT. Magnified views of the center (Fig. S6K) and edges (Fig. S6J and Fig. S6L) revealed that sarcomeres were more aligned at the edges of the tissue than at the center. Overall, we observed some degree of alignment in the longitudinal direction, but this alignment was localized to the edges or borders of the tissues. Additionally, we observed diagonal alignment at the corners of the EHTs generated in cylindrical or stadium-like cavities.

VI. CONTRACTILE DISPLACEMENTS IN 2D

In estimating the effective spring constant of the platform experienced by the EHTs, we assumed a contractile force that is normal from the surface of the attachment sites. This is in the x direction for uniaxial tissues, and in the r for the cylindrical and stadium-like cavities (Fig. S3). However, modeling a normal force using a cylindrical coordinate system may not be entirely accurate in estimating the spring constant for longer tissues in stadium-like configurations, particularly for diagonally oriented attachment sites. In other words, the assumption of $F_x = F_y = F\sin(45°)$ may not be valid for 45° oriented cages in the longer tissues. Although we calculated the total displacement through-

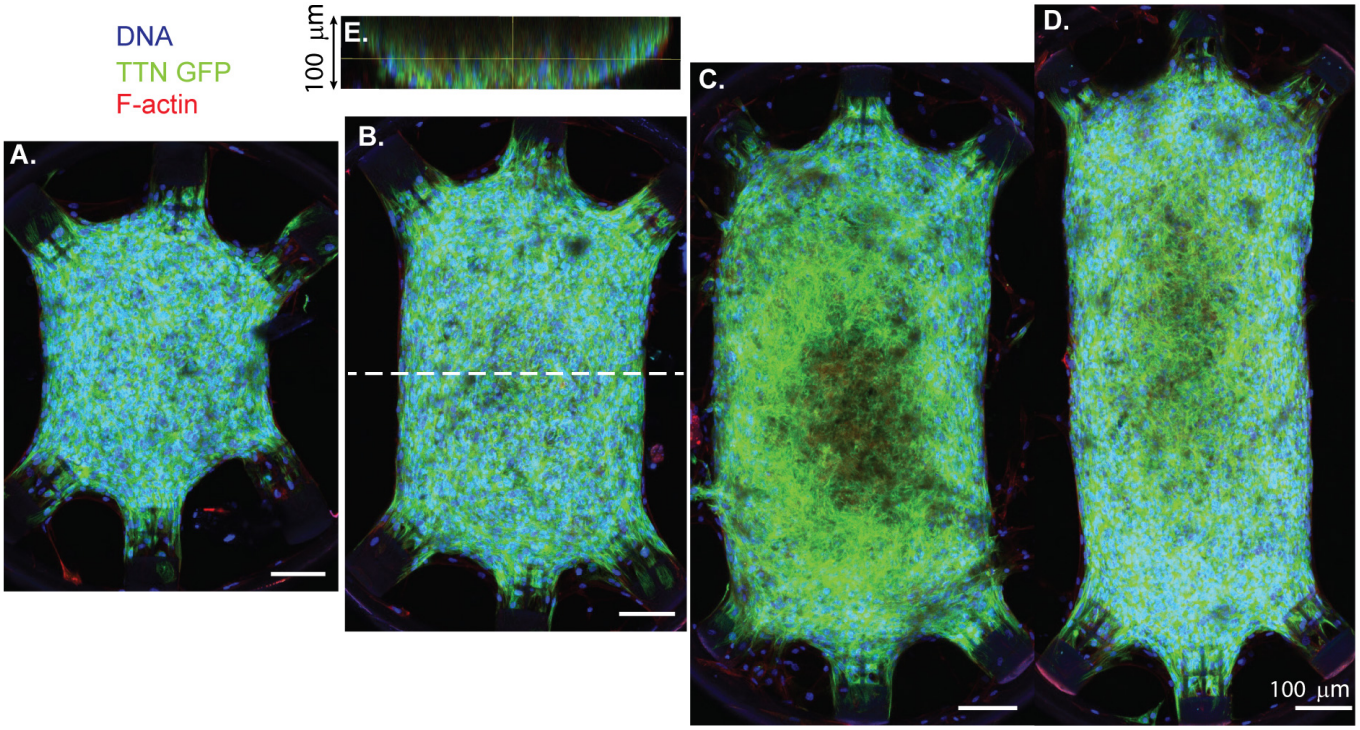

FIG. S5: Immunofluorescent staining of EHTs with nuclei (blue), TTN-GFP (green), and F-actin (red) in stadium-like cavities show the tissue structure and its thickness. (A-D) display maximum projections of the 0.8 mm, 1 mm, 1.2 mm, and 1.4 mm long tissues respectively. (E) shows the cross-section of the 1 mm long EHT (dashed line), which indicates > 100 μm thickness. Scale bars are 100 μm.

out the main text, our MATLAB-based displacement tracking algorithm can resolve the absolute cage movements in x and y directions.

Fig. S7A shows a representative trace taken from monitoring a diagonally oriented cage (top left) of a 1.2 mm long tissue, where there is a > 5 fold difference between the displacements in x and y directions. To further investigate, we plotted the x and y components of the displacement in Fig. S7B for all diagonal cages. Results reveal that the lengthwise component of the displacement is significantly more than the orthogonal component for 1.2 mm and 1.4 mm long tissues with > 2 aspect ratio. The forces these tissues exert on diagonal attachment sites can no longer be considered normal stresses. Therefore, while it is not a part of this study, more sophisticated modeling is required to take into account 2D forces, the resulting rotational motion of the cages, and its associated spring constant.

VII. EXPERIMENT WITH THE GSB-L550 CELL LINE

We used a device with uniaxial configuration to generate and test EHTs from another human induced pluripotent stem cell line. GSB-L550 (Greenstone Biosciences) cell line is differentiated to the cardiomyocytes using a similar protocol, then cardiomyocytes are mixed with human mesenchymal stem cells and collagen, and centrifuged into the rectangular cavities to generate EHTs. We show these EHTs in Movie S4 and results in Fig. S8. Overall, all these EHTs achieved stability (Movie S4), and we observed an increase in applied force as length of the EHTs were increased. However, slight increase in force between 1 mm long and 2 mm long tissues indicate a similar converging trend with respect to the PGP1 cell line we tested with uniaxial configuration (Fig. 6G). When we were observing GSB-L550 tissues over time (Fig. S8A-B), we noticed an increase in contractile performance of 1 mm and 2 mm long EHTs, and a decrease for 0.5 mm EHT.

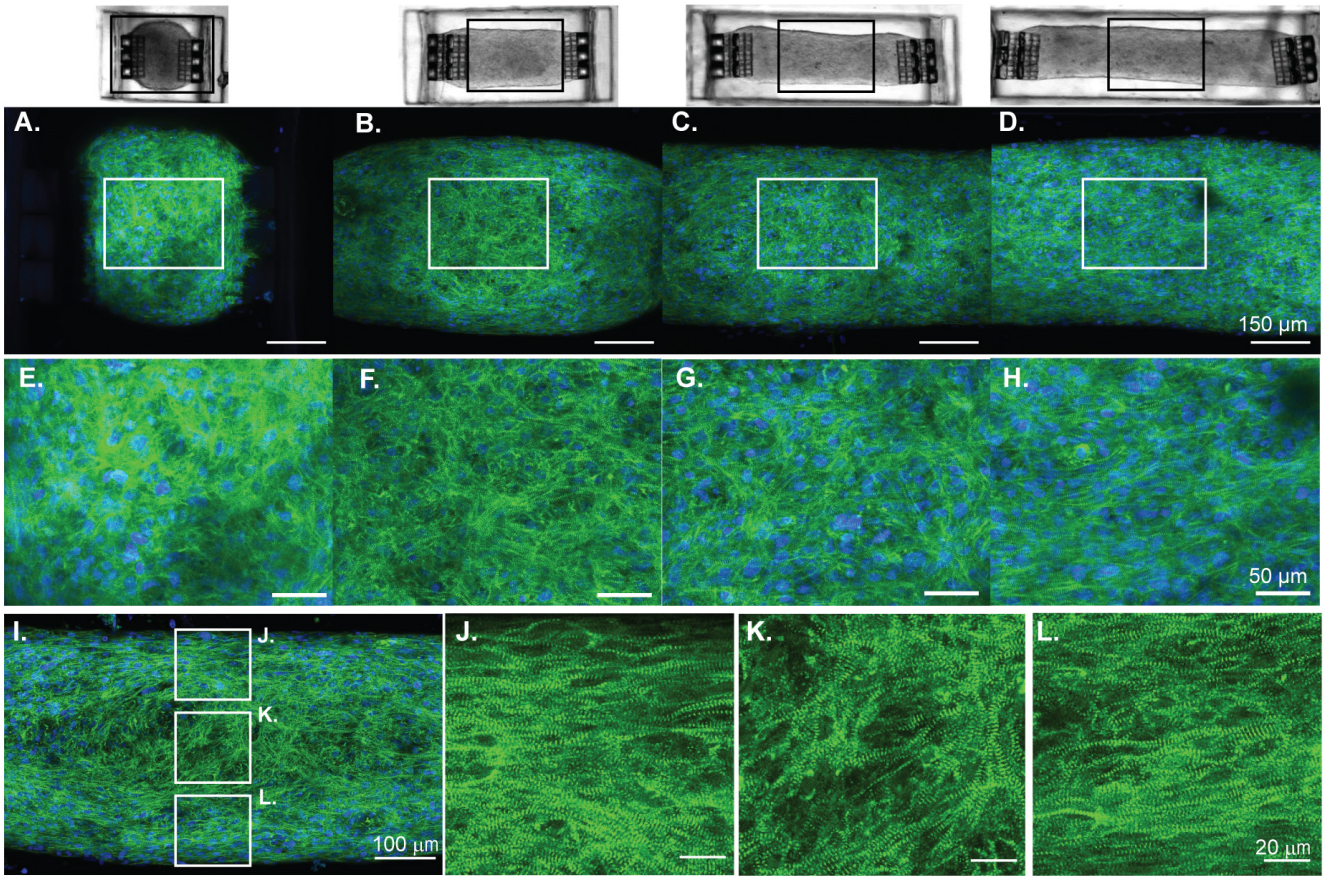

FIG. S6: Immunofluorescent staining with nuclei (blue) and TTN-GFP (green) reveal the fiber structure in rectangular EHTs. (A-D) shows brightfield images of the 0.5 mm, 1 mm, 1.5 mm, and 2 mm long tissues (top), where rectangular boxes are magnified and shown as immunofluorescent images (bottom, scale bar is 150 μm). (E-H) represent further magnification of center regions of 0.5 mm, 1 mm, 1.5 mm, and 2 mm long EHTs respectively (scale bars are 50 μm). (I) displays a center region of another 2 mm long EHT (scale bar is 100 μm), where the (J), (K), and (L) show magnified views of the top edge, center, and bottom edge respectively (scale bar is 20 μm).

VIII. EFFECT OF THE CAGE LENGTH ON CONTRACTILE FORCE

We picked the 1 mm long seeding well as a testbed to study and compare the effect of doubling the length of the attachment sites. We present 3 combinations: the EHTs between short cages ("singles"), between long cages ("doubles"), and the asymmetric combination in which there are short cages on one side and long cages on the other side. When we compare the forces generated in tissues between short and long attachment sites (see S9A), we observed higher deflection from the longer cages, thus the generated force was larger. Unfortunately, only one tissue for each configuration was available on the same chip for this comparison, so further investigation with more tissues is needed. In Fig. S9B, we study and compare the forces exerted upon single cages versus cages that are doubled in length, across 5 different EHTs (Day 8) with asymmetric configuration (Fig. S9A, bottom). In all of them except one, the deflections observed from longer cages were larger than the ones reported from the shorter attachment sites. If the tissues are completely suspended between the attachment sites, there shouldn't be a major difference in the forces measured from either side of the tissue, due to the force balance. To further investigate this, we look back and investigate the temporal evolution of force difference from Day 6 and Day 8 in Fig. S9D. Here, the forces exerted upon the attachment sites for the same tissues were collapsed and compared. The force difference between both sides of the same tissues was small and tolerable on Day 6, but it became more pronounced over the course of 2 days. The force imbalance can normally be a sign of inaccurate estimation and variability of effective spring constant k_{eff} between boundary to boundary. The partial detachment of flexible membranes from the bottom surface between Day 6 to Day 8, particularly for the membranes that host the long attachment sites can explain this difference. Another reason can be the increased surface area provided by the cages that are doubled in length. It is likely that cells in

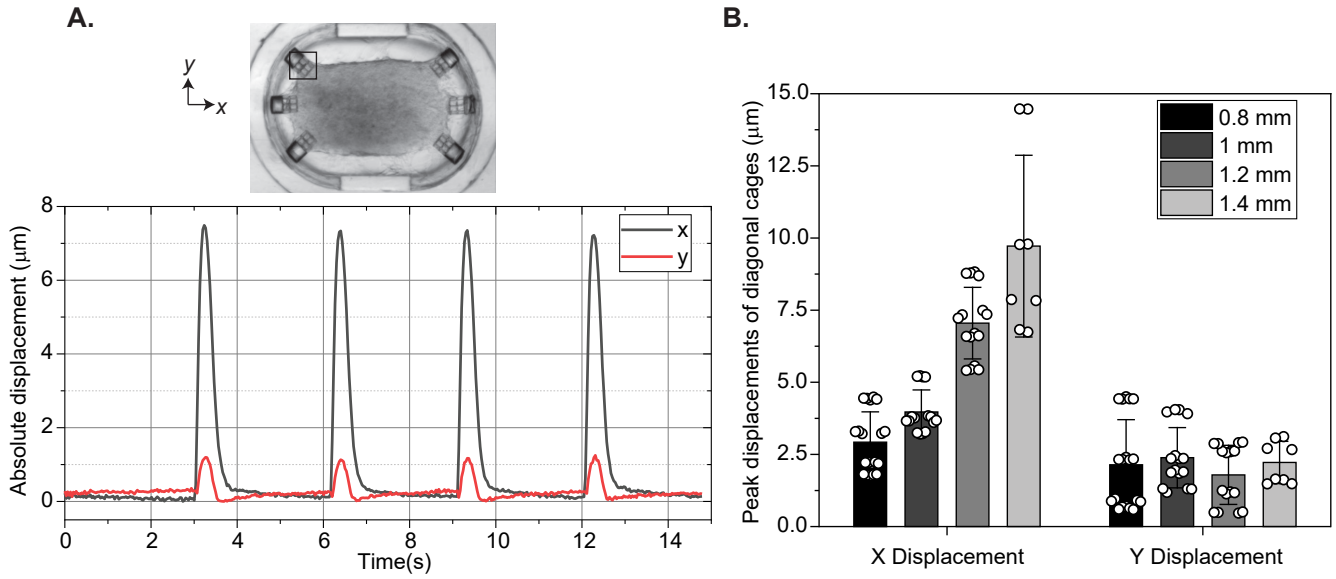

FIG. S7: x and y components of the contractile motion on diagonal cages. (A) shows the displacements of a diagonal cage (top inset, empty square) during spontaneous contractions of a 1.2 mm long tissue. (B) shows the peak displacements of all diagonal cages in x and y directions, where x is the lengthwise direction (PGP1 cell line is used to generate these tissues).

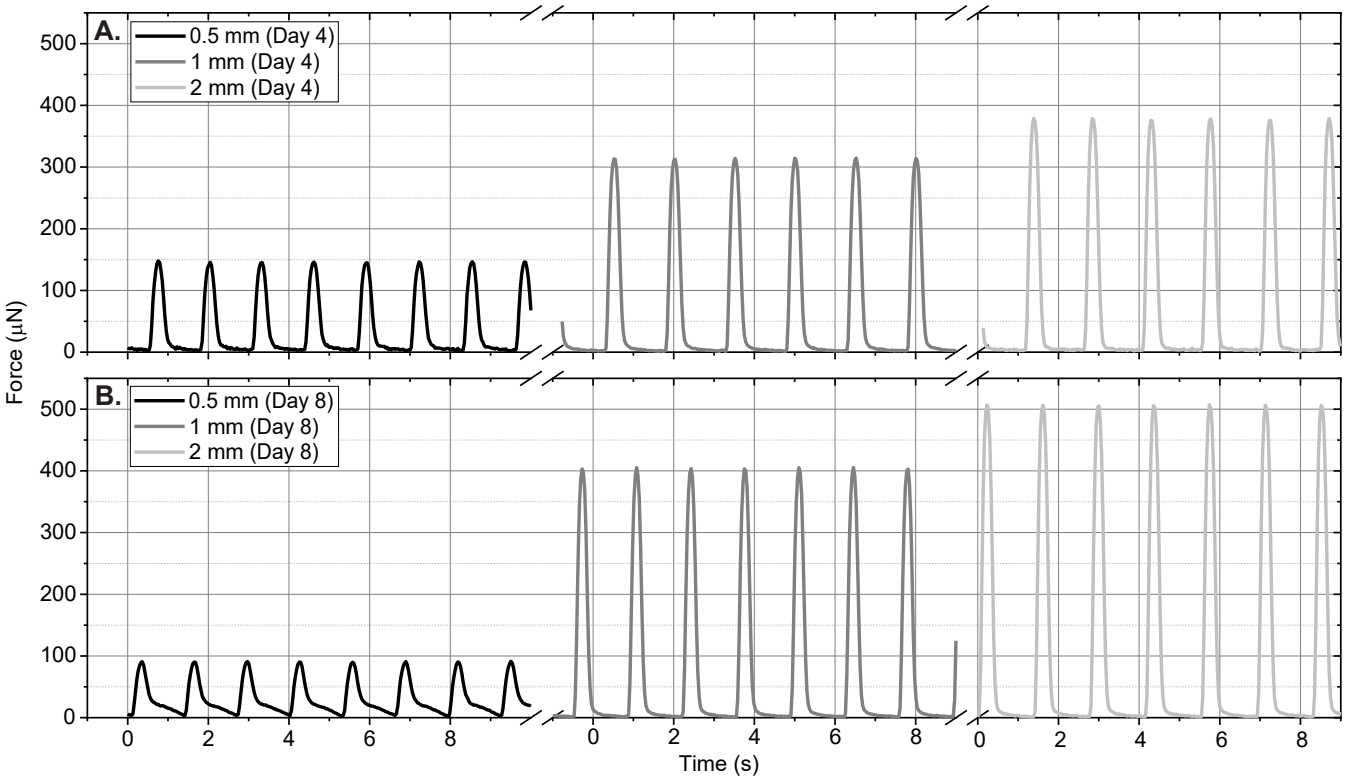

FIG. S8: Spontaneous contractions of EHTs generated from GSB-L550 cell line, in soft rectangular cavities. Forces exerted from the left and right sides of the 0.5 mm, 1 mm, and 2 mm long EHTs in (A) Day 4 and (B) Day 8 were analyzed and averaged to obtain the plots.

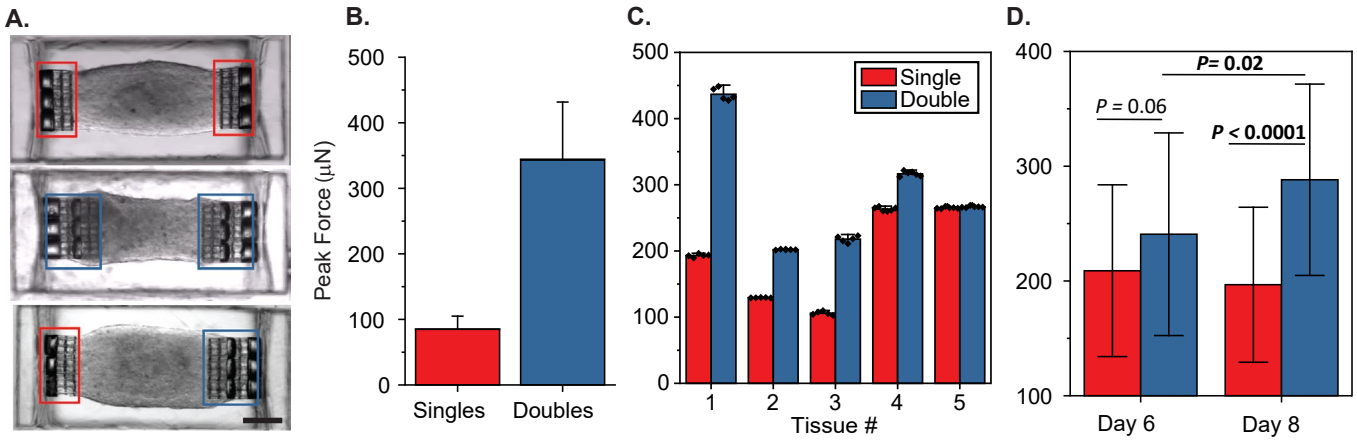

FIG. S9: A) shows brightfield images of 1 mm long tissues generated between short cages (singles, top), long cages (doubles, middle), and asymmetric cages (single and double, bottom). Red and blue boxes denote regions of interest for the force estimation, and the scale bar is 200 μm. (B) Compares peak forces exerted upon cages in (A, top) and (A, middle) on Day 8. (C) compares forces at mechanical boundaries for the EHTs generated in the asymmetric configuration on Day 8. (D) merges the data in (C), but also shows the temporal evolution of forces from Day 6 to Day 8. The data points are shown with means and + or ±1 SD on plots; Student's t test, $\alpha = 0.05$.

EHTs are redistributed more to the long cages than the short ones during tissue remodeling (Fig. S9A), leading to an increase in force that is locally exerted upon cages. Although we didn't investigate this phenomenon further, our approach and fabrication method allowed us to study the effects of asymmetry and mechanical nonuniformities upon uniaxially contracting EHTs in addition to length.

IX. CALCIUM DYNAMICS

Oscillations of calcium concentrations within the heart excite the mechanical contractions and they are one of the key drivers of the heart function [2]. Thus, measuring the calcium dynamics in the cardiac EHTs for the entire range of physiological beating frequencies can give us important information about the functioning and physiology of the engineered heart tissues in this study. Figure S11 shows an example where we demonstrate the simultaneous recording of mechanical contractions and calcium transients for a single contraction-relaxation cycle for both 0.8 mm and 1.2 mm long tissues. In order to assess the calcium handling as a function of frequency, we performed nearly the same electrical pacing protocol, with two exceptions. Motivated by the most recent electrical stimulation regimens in the literature [3, 4], we doubled the excitation frequencies to $1, 2, 3, 4, 5$ Hz. Second, we didn't repeat the stimulation protocol after the end of the 5 Hz cycles. The relative fluorescence amplitudes, F/F_0, which inform us about calcium oscillations across these frequencies, are shown in Fig.S11E-F. For these measurements, we take into account the entire field of view containing the boundaries of the tissues. Both of these EHTs were able to keep up with the pacing up to 5 Hz. However, the amplitude of the active oscillations decreased as a function of frequency for both cases. At the end of the protocol, we observed a drop below the baseline, which might indicate the depletion of calcium stores in the cardiomyocytes. For example, the 0.8 mm tissue couldn't recover the baseline value during the 20-second rest period after the end of the protocol, but it seems like the calcium concentration is increasing within the tissue in this period. Sufficient calcium accumulation over time might still trigger a calcium-induced calcium release in the 30 seconds or so (based on the slope) and cause a spontaneous contraction [2, 5]. We also observe that the spontaneous beating frequency of 1.2 mm long tissue is higher (Fig.S11H), which implies a faster charging or recovery time after a beat without the electrical stimulation. In Fig.S11G, we compare the full-width half-maximum (FWHM) of the fluorescence oscillations, which is a calcium analog of contraction duration (t50) values, over the course of the experiment. Even though we used a wider (or longer) field of view for the analysis of the 1.4 mm long tissue, we observed nearly the same values reflecting the temporal qualities of calcium transient between $3 - 5$ Hz. In lower frequencies, FWHM seems to be slightly larger in the shorter EHT. Considering the fact that the speed of the calcium waves is also proportional to $\Delta F/L$ where L is the length of the measured area, it seems likely that the calcium transients propagate faster in the longer tissue with the higher aspect ratio [6].

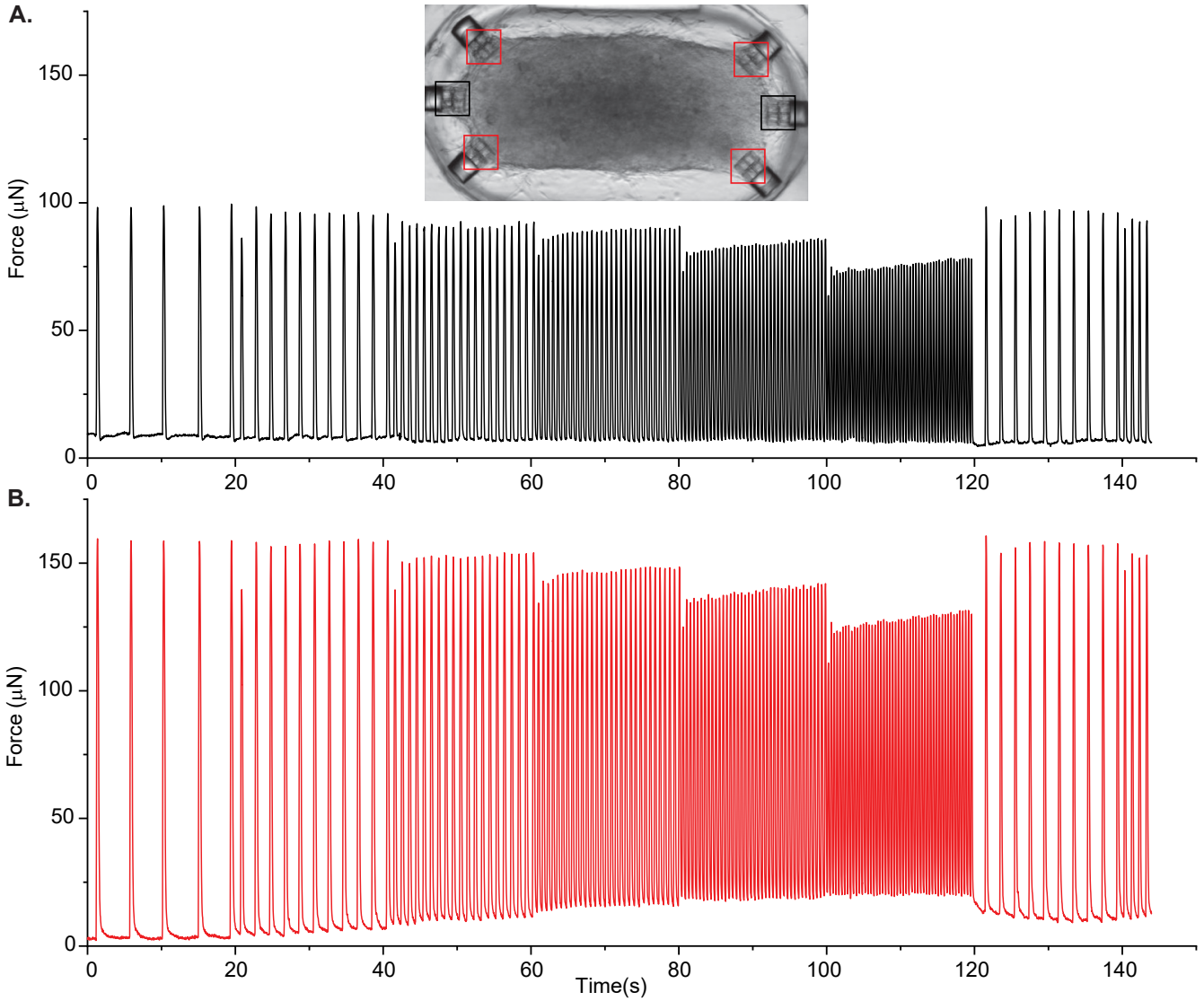

FIG. S10: Frequency-dependent contractile behavior of the 1.4 mm EHT generated in a stadium-like seeding well. Force recording of a 1.4 mm EHT during electrical stimulation, generated by tracking and averaging the displacements of the 0° oriented (A) and diagonally oriented (B) attachment sites. The inset shows an image of 1.4 mm long EHT, where black (A) and red (B) squares show regions of interest for the analysis. The tissues were stimulated for 20 seconds at 0.5 Hz, 1 Hz, 1.5 Hz, 2 Hz, 2.5 Hz, and back to the 0.5 Hz, starting from 20 seconds.

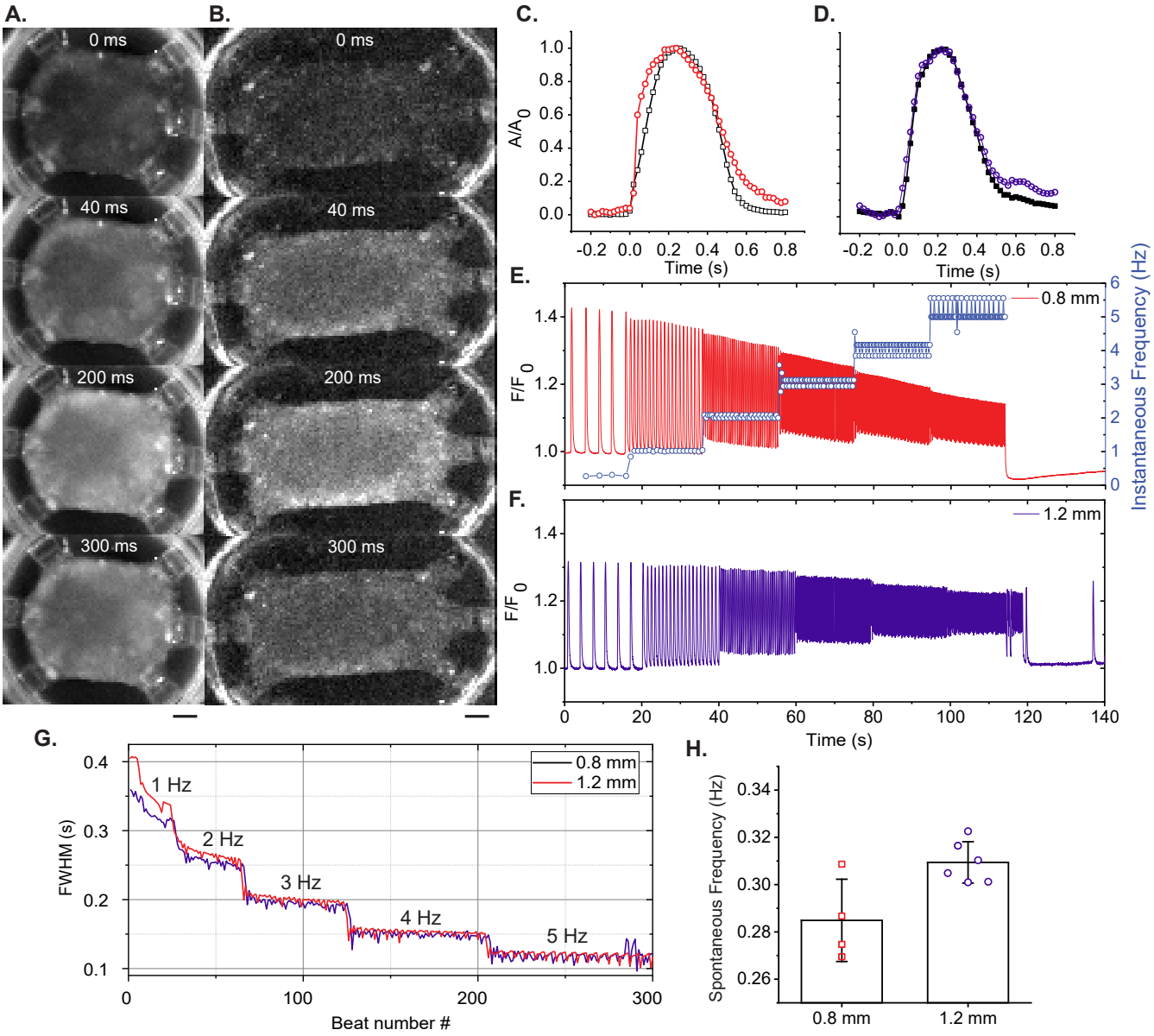

FIG. S11: (A) and (B) show the time series fluorescence images of EHTs generated in 0.8 mm long and 1.2 mm long stadium-like cavities respectively, after incubation with calcium indicator Fluo-4. The scale bar is 100 μm. (C) and (D) display simultaneous recording of the fluorescence of the calcium indicator and a period of contractile motion for 0.8 mm long (fluorescence: red) and 1.2 mm long tissues (fluorescence: violet). (E) and (F) show recording of calcium dynamics during electrical stimulation of 0.8 mm and 1.2 mm long cardiac EHTs (starting from 20 s, paced at 1, 2, 3, 4, and 5 Hz, 20 seconds each). (G) Full-width half maximums (FWHM) of calcium oscillations for 0.8 mm and 1.2 mm long cardiac EHTs. (H) Spontaneous beating frequencies of the EHTs before the experiment.

X. SUPPLEMENTARY MOVIES

A. Movie S1

Spontaneously beating 0.5 mm (left), 1 mm (center), and 1.5 mm (right) long, uniaxially engineered heart tissues, generated in "stiff" platform (Day 9).

B. Movie S2

Spontaneously beating engineered heart tissues, generated in uniaxial configuration.

C. Movie S3

Spontaneously beating engineered heart tissues, generated in stadium-like configuration.

D. Movie S4

Spontaneously beating engineered heart tissues created from GSB-L550 hiPSC line (left: Day 4, right: Day 8), in uniaxial configuration.

E. Movie S5

Calcium imaging of the engineered heart tissues, at a pacing frequency of 1 Hz.

[1] R. K. Jayne, M. Ç. Karakan, K. Zhang, N. Pierce, C. Michas, D. J. Bishop, C. S. Chen, K. L. Ekinci, and A. E. White, Lab on a Chip **21**, 1724 (2021).
[2] D. M. Bers, Nature **415**, 198 (2002).
[3] K. Ronaldson-Bouchard, S. P. Ma, K. Yeager, T. Chen, L. Song, D. Sirabella, K. Morikawa, D. Teles, M. Yazawa, and G. Vunjak-Novakovic, Nature **556**, 239 (2018).
[4] K. Ronaldson-Bouchard, K. Yeager, D. Teles, T. Chen, S. Ma, L. Song, K. Morikawa, H. M. Wobma, A. Vasciaveo, E. C. Ruiz, et al., Nature protocols **14**, 2781 (2019).
[5] O. Cohen and S. A. Safran, Physical review letters **122**, 198101 (2019).
[6] A. P. Petersen, N. Cho, D. M. Lyra-Leite, J. W. Santoso, D. Gupta, N. R. Ariyasinghe, and M. L. McCain, Integrative Biology **12**, 34 (2020).